

# Constraining the state of the intergalactic medium during the Epoch of Reionization using MWA 21-cm signal observations

Raghunath Ghara<sup>1,2\*</sup>, Sambit K. Giri<sup>3†</sup>, Benedetta Ciardi<sup>4</sup>, Garrelt Mellema<sup>5</sup>, and Saleem Zaroubi<sup>1,6,2</sup>

<sup>1</sup>ARCO (Astrophysics Research Center), Department of Natural Sciences, The Open University of Israel, 1 University Road, PO Box 808, Ra'anana 4353701, Israel

<sup>2</sup>Department of Physics, Technion, Haifa 32000, Israel

<sup>3</sup>Institute for Computational Science, University of Zurich, Winterthurerstrasse 190, 8057 Zurich, Switzerland

<sup>4</sup>Max-Planck Institute for Astrophysics, Karl-Schwarzschild-Straße 1, 85748 Garching, Germany

<sup>5</sup>The Oskar Klein Centre, Department of Astronomy, Stockholm University, AlbaNova, SE-10691 Stockholm, Sweden

<sup>6</sup>Kapteyn Astronomical Institute, University of Groningen, PO Box 800, 9700AV Groningen, the Netherlands

Accepted XXX. Received YYY; in original form ZZZ

## ABSTRACT

The Murchison Widefield Array (MWA) team has derived new upper limits on the spherically averaged power spectrum of the 21-cm signal at six redshifts in the range  $z \approx 6.5 - 8.7$ . We use these upper limits and a Bayesian inference framework to derive constraints on the ionization and thermal state of the intergalactic medium (IGM) as well as on the strength of a possible additional radio background. We do not find any constraints on the state of the IGM for  $z \gtrsim 7.8$  if no additional radio background is present. In the presence of such a radio background, the 95 per cent credible intervals of the disfavoured models at redshift  $\gtrsim 6.5$  correspond to an IGM with a volume averaged fraction of ionized regions below 0.6 and an average gas temperature  $\lesssim 10^3$  K. In these models, the heated regions are characterised by a temperature larger than that of the radio background, and by a distribution with characteristic size  $\lesssim 10 h^{-1}$  Mpc and a full width at half maximum (FWHM) of  $\lesssim 30 h^{-1}$  Mpc. Within the same credible interval limits, we exclude an additional radio background of at least 0.008% of the CMB at 1.42 GHz.

**Key words:** radiative transfer - galaxies: formation - intergalactic medium - cosmology: theory - dark ages, reionization, first stars - X-rays: galaxies

## 1 INTRODUCTION

During the Epoch of Reionization (EoR) ultra-violet (UV) radiation from the earliest generations of galaxies ionized the primordial neutral hydrogen (H I) in the intergalactic medium (IGM). This global phase transition permanently changed the state of the IGM and had far reaching consequences for the subsequent formation and evolution of galaxies. Observations of the absorption spectra of quasars at redshift  $z \gtrsim 6$  (e.g. Fan et al. 2006; Bañados et al. 2018; Davies et al. 2018; Greig et al. 2017, 2019; Wang et al. 2020; Yang et al. 2020) and the measurement of the Thomson scattering optical depth from observations of the Cosmic Microwave Background (CMB) (Planck Collaboration et al. 2020) suggest that this transition took place sometime between redshift  $\approx 6$  and 10 (e.g. Mitra et al. 2015). However, many of its details, such as the exact timing of the process, the ionization and thermal state of the IGM, the morphology of the ionized regions, remain poorly understood (see e.g. Pritchard & Loeb 2012; Zaroubi 2013, for reviews).

The 21-cm signal produced by H I in the IGM is the most direct probe of the reionization process as it depends directly on the H I density. It is therefore expected to answer many of the outstanding questions, including the nature of the sources responsible for reionization. Thus, substantial efforts have been made to measure this signal. Observations of the 21-cm signal fall into two categories. The first type uses large interferometric radio telescopes to measure the statistical fluctuations of the signal. Examples of such telescopes are the Low Frequency Array (LOFAR)<sup>1</sup> (van Haarlem et al. 2013; Patil et al. 2017), the Precision Array for Probing the Epoch of Reionization (PAPER)<sup>2</sup> (Parsons et al. 2014; Kolopanis et al. 2019), the Murchison Widefield Array (MWA)<sup>3</sup> (e.g. Tingay et al. 2013; Wayth et al. 2018), the New extension in Nançay Upgrading loFAR (NenuFAR)<sup>4</sup> (Zarka et al. 2012), the Upgraded Giant Metrewave Radio Telescope (uGMRT) (Gupta et al. 2017), the Owens

\* E-mail: ghara.raghunath@gmail.com

† E-mail: sambit.giri@gmail.com

<sup>1</sup> <http://www.lofar.org/>

<sup>2</sup> <http://eor.berkeley.edu/>

<sup>3</sup> <http://www.mwatelescope.org/>

<sup>4</sup> <https://nenufar.obs-nancay.fr/>

Valley Radio Observatory Long Wavelength Array (OVRO-LWA)<sup>5</sup> and the Hydrogen Epoch of Reionization Array (HERA)<sup>6</sup> (DeBoer et al. 2017). A more sensitive radio interferometer, the upcoming Square Kilometre Array (SKA)<sup>7</sup>, should be able to also produce tomographic images of the distribution of the signal on the sky (Mellema et al. 2015; Ghara et al. 2017; Giri et al. 2018a,b; Giri Giri; Ghara & Choudhury 2020; Giri & Mellema 2020; Kapahtia et al. 2021). The second type of observations use single antennae and attempt to measure the sky-averaged 21-cm signal and its evolution with time. Examples are EDGES (Bowman & Rogers 2010), EDGES2 (Monsalve et al. 2017; Bowman et al. 2018), SARAS (Patra et al. 2015), SARAS2 (Singh et al. 2017), SARAS3 (Nambissan et al. 2021), PRIZM (Philip et al. 2019), BigHorns (Sokolowski et al. 2015), SciHi (Voytek et al. 2014) and LEDA (Price et al. 2018).

One of the main challenges of these experiments is to remove the contribution of the galactic and extra-galactic foregrounds, which is stronger than the expected 21-cm signal by several orders of magnitude. Their smooth frequency dependence should allow a separation from the fluctuating 21-cm signal, allowing them to be either subtracted (Harker et al. 2009; Bonaldi & Brown 2015; Chapman et al. 2016; Mertens et al. 2018; Hothi et al. 2021), suppressed (Datta et al. 2007; Majumdar et al. 2012; Ghara et al. 2016) or avoided (Datta et al. 2010; Liu et al. 2014). Moreover, an exquisite calibration of the system is required to minimize the artefacts from strong sources (Barry et al. 2016; Patil et al. 2017), and a long observation time is necessary to reduce the instrumental noise. Further calibration challenges may be posed by the hardware components of the telescope (see e.g., Kern et al. 2019) and by the temporally and spatially varying ionosphere (see e.g., Mevius et al. 2016), to mention a few.

So far, no undisputed detection of the 21-cm signal from the EoR has been achieved. Bowman et al. (2018) analysed observations with the EDGES2 low-band antenna and claimed a detection of the averaged brightness temperature of the 21-cm signal ( $\delta T_b$ ) at various redshifts. The redshift evolution of  $\delta T_b$  has a minimum at  $z \approx 17$  with an amplitude much stronger than predicted by standard theories. Therefore the validity of these claims have been debated (e.g. in Hills et al. 2018; Draine & Miralda-Escudé 2018; Singh & Subrahmanyan 2019; Bradley et al. 2019), and unconventional physical processes such as an unknown cooling mechanism (see e.g., Tashiro et al. 2014; Barkana 2018; Fialkov et al. 2018; Muñoz & Loeb 2018; Ghara & Mellema 2020) or the presence of an additional radio background on top of the CMB (Feng & Holder 2018; Ewall-Wice et al. 2018; Fialkov & Barkana 2019; Mebane et al. 2020) have been invoked to explain these results.

While none of the other attempts have to date claimed a detection of the signal, several of them have provided upper limits. A  $2\sigma$  value of  $\Delta^2(k) < (248)^2 \text{ mK}^2$  for a  $k$ -scale  $0.5 h \text{ Mpc}^{-1}$  was the very first upper limit on the power spectrum<sup>8</sup> of the 21-cm signal from redshift 8.6, obtained from observations with the GMRT (Paciga et al. 2013). Barry et al. (2019), Cheng et al. (2018), and Kolopanis et al. (2019) provided upper limits using the observations with MWA and PAPER. Patil et al. (2017) published the first

upper limit on the power spectrum of the signal from redshift between 9.6 and 10.6 using LOFAR observations. Later, Gehlot et al. (2019, 2020) and Eastwood et al. (2019) probed a higher redshift range and also provided upper limits on the power spectrum using observations with the LOFAR-Low Band Antenna array and the OVRO-LWA, respectively. Recently, Mertens et al. (2020) analysed 10 nights of LOFAR observations of the North Celestial Pole and obtained a  $2\sigma$  upper limit on the 21-cm signal power spectrum at  $z \approx 9.1$  of  $\Delta^2(k = 0.075 h \text{ Mpc}^{-1}) = (73)^2 \text{ mK}^2$ .

The focus of this paper is on the upper limits in the redshift range 6.5 – 8.7 published by the MWA team (Trott et al. 2020). Their best  $2\sigma$  upper limit at redshift 6.5 is  $\Delta^2(k = 0.14 h \text{ Mpc}^{-1}) \approx (43)^2 \text{ mK}^2$ , derived from 110 hours of integration with the MWA high band on the EoR0 field. The upper limit values increase with redshift. At  $z = 8.7$ , the upper limit of  $\Delta^2(k = 0.14 h \text{ Mpc}^{-1}) \approx (250)^2 \text{ mK}^2$  comes from 51 hours of observations of the EoR2 field.

The emitted 21-cm signal from H I depends on the number density of the sources present at those epochs, as well as on the emissivity of UV, X-ray, radio and Ly $\alpha$  photons from those sources (see e.g., Ross et al. 2019; Reis et al. 2020a). Due to the complex dependence of the signal on the sources, it is not straightforward to extract the astrophysical as well as the cosmological information from 21-cm signal observations, and exploration of many theoretical models of the signal is required to interpret the results. Often, the signal prediction algorithms are used in a Bayesian inference framework to explore the parameter space of the reionization models (e.g. Greig & Mesinger 2015; Greig & Mesinger 2017; Park et al. 2019; Cohen et al. 2020; Ghara et al. 2020; Mondal et al. 2020; Greig et al. 2021a,b).

In this paper, we consider the new upper limits on the 21-cm signal power spectrum from MWA observations (Trott et al. 2020) in the redshift range spanning from 6.5 to 8.7 to constrain the IGM conditions and explore scenarios for the EoR that are disfavoured by such limits. Our framework is based on simulations of the power spectrum and IGM parameters and a Bayesian inference framework. Just as in our work on the LOFAR upper limits for  $z \approx 9.1$  (Ghara et al. 2020), our main focus is on deriving constraints on the condition of the IGM. In addition, we also aim to put constraints on the additional radio background which has been proposed to explain the EDGES2 results. This work differs from the interpretation of the MWA upper limits by Greig et al. (2021a), who instead focused on the properties of the sources and did not consider any additional radio background component to the CMB.

This paper is structured as follows. In Section 2, we describe the basic methodology of our framework. We present our results in Section 3. We discuss the outcome of this study from the point of view of other observations in Section 4, before concluding in Section 5. The cosmological parameters used throughout this study are the same of the  $N$ -body simulations employed here, i.e.  $\Omega_m = 0.27$ ,  $\Omega_\Lambda = 0.73$ ,  $\Omega_B = 0.044$ ,  $h = 0.7$  (Wilkinson Microwave Anisotropy Probe (WMAP); Hinshaw et al. 2013).

## 2 FRAMEWORK

Here we describe the framework employed to constrain the IGM properties using the observational upper limits from the MWA.

### 2.1 Modelling the 21-cm signal using GRIZZLY

Our framework uses the GRIZZLY code (Ghara et al. 2015a, 2018) to generate 21-cm signal maps for the redshift range  $z \approx 6.5 - 8.7$

<sup>5</sup> <http://www.tauceti.caltech.edu/LWA/>

<sup>6</sup> <https://reionization.org/>

<sup>7</sup> <http://www.skatelescope.org/>

<sup>8</sup> Here and for the rest of this paper we use the so-called dimensionless form of the power spectrum,  $\Delta^2(k)$ , which is related to the standard spherically averaged power spectrum  $P(k)$  through  $\Delta^2(k) = k^3 P(k) / 2\pi^2$ .

**Table 1.** Overview of the simulation parameters used in GRIZZLY and their explored ranges.

Simulation Parameters	Description	Explored range
$\zeta$	Ionization efficiency	$[10^{-3}, 10^3]$
$M_{\min}$	Minimum mass of the UV emitting halos	$[10^9 M_{\odot}, 10^{12} M_{\odot}]$
$M_{\min,X}$	Minimum mass of the X-ray emitting halos	$[10^9 M_{\odot}, 10^{12} M_{\odot}]$
$f_X$	X-ray heating efficiency	$[10^{-3}, 10^2]$
$A_r$	Efficiency of the excess radio background	$[0, 416]$

for different combinations of astrophysical parameters. The code requires gridded versions of cosmological density fields and halo catalogues as input. We use density fields of length  $500 h^{-1}$  comoving megaparsec (Mpc) smoothed onto  $300^3$  grids (see e.g. [Giri et al. 2019a,b; Kamran et al. 2021](#)), which were retrieved from the results of the PRACE<sup>9</sup> project PRACE4LOFAR. This box size corresponds to a field-of-view of  $4.3^\circ \times 4.3^\circ$  at redshift  $\approx 9$ . The minimum mass of the dark matter halos as identified on the fly with a spherical overdensity halo finder ([Watson et al. 2013](#)) is  $\approx 10^9 M_{\odot}$ . These are the same cosmological  $N$ -body simulation previously used in [Ghara et al. \(2020\)](#).

The GRIZZLY code is an independent implementation of the previously developed BEARS algorithm ([Thomas & Zaroubi 2008; Thomas et al. 2009; Thomas & Zaroubi 2011; Krause et al. 2018](#)). It is based on a one-dimensional radiative transfer scheme which approximates the transfer of photons (UV, X-rays and Ly $\alpha$ ) by assuming that the effect from individual sources is isotropic. We refer the reader to the original papers ([Ghara et al. 2015a, 2018](#)) for a more detailed and complete description of the algorithm.

Given a set of astrophysical source parameters, GRIZZLY generates ionization and gas temperature maps at different redshifts which are then used to produce differential brightness temperature ( $\delta T_b$ ) maps. The  $\delta T_b$  of the 21-cm signal can be expressed as (see e.g. [Madau et al. 1997; Furlanetto et al. 2006](#)),

$$\begin{aligned} \delta T_b(\mathbf{x}, z) &= 27 x_{\text{HI}}(\mathbf{x}, z) [1 + \delta_B(\mathbf{x}, z)] \left( \frac{\Omega_B h^2}{0.023} \right) \\ &\times \left( \frac{0.15}{\Omega_m h^2} \frac{1+z}{10} \right)^{1/2} \left( 1 - \frac{T_{\gamma, \text{eff}}}{T_S(\mathbf{x}, z)} \right) \text{mK}, \end{aligned} \quad (1)$$

where  $x_{\text{HI}}$  and  $\delta_B$  denote the neutral hydrogen fraction and baryonic density contrast respectively, each at position  $\mathbf{x}$  and redshift  $z$ . The quantity  $T_{\gamma, \text{eff}}$  is the temperature of the radio background, which reduces to the usual CMB temperature,  $T_{\gamma}(z) = 2.725 (1+z)$  K, in the absence of additional contributions. We assume that the spin temperature of hydrogen in the IGM,  $T_S$ , is equal to the gas temperature. This condition occurs in the presence of a strong Ly $\alpha$  background which is expected at the redshifts of interest (e.g. [Barkana & Loeb 2005; Pritchard & Loeb 2012; Schneider et al. 2020](#)).

Afterwards we calculate the dimensionless power spectrum of  $\delta T_b$ , denoted as  $\Delta^2(k)$ . Note that we have ignored the presence of redshift space distortions (RSD) while evaluating the power spectrum for different model parameters, as their impact remains rather small during the epoch of our interest<sup>10</sup>, when ionization fluctu-

ations dominate the power spectrum of  $\delta T_b$  ([Jensen et al. 2013; Majumdar et al. 2016; Ghara et al. 2015a,b; Ross et al. 2020](#)).

## 2.2 Simulation parameters in GRIZZLY

GRIZZLY uses the following set of parameters to generate the maps of ionization fraction and gas temperature in the IGM. These are later used to generate  $\delta T_b$  maps and from these the power spectra. We describe the parameters below and summarise the range of values explored in Table 1.

- Ionization efficiency ( $\zeta$ ): This scales the rate of emission of ionizing photons per unit stellar mass from a halo  $\dot{N}_i$  as  $\dot{N}_i = \zeta \times 2.85 \times 10^{45} \text{ s}^{-1} M_{\odot}^{-1}$ .  $\zeta = 1$  corresponds to a model galaxy spectrum which has been produced with the publicly available population synthesis code PEGASE2<sup>11</sup> ([Fioc & Rocca-Volmerange 1997](#)) and employed in the 1D radiative transfer. We assume that the stellar mass  $M_{\star}$  of a halo is related to the dark matter halo mass  $M_{\text{halo}}$  as  $M_{\star} = f_{\star} \frac{\Omega_B}{\Omega_m} M_{\text{halo}}$ , where the star formation efficiency  $f_{\star}$  is fixed at 0.02 ([Behroozi & Silk 2015; Sun & Furlanetto 2016](#)). Note that the effect of  $\zeta$  is degenerate with that of  $f_{\star}$ , the emission rate of ionizing photons from the sources, and their escape fraction into the IGM. Here we vary  $\text{Log}_{10}(\zeta)$  between  $[-3, 3]$ .

- Minimum mass of the UV emitting halos ( $M_{\min}$ ): We assume no emission of ionizing photons from halo with mass less than  $M_{\min}$ . This is to incorporate the fact that various mechanism such as the radiative and mechanical feedback can reduce the star formation efficiency significantly (see e.g., [Hasegawa & Semelin 2013; Dawoodbhoy et al. 2018](#)). In general, one expects that the radiative feedback suppresses star formation in halos with mass  $\lesssim 10^9 M_{\odot}$  (see e.g., [Wise et al. 2014; Dixon et al. 2016](#)). In our study the lowest value for  $M_{\min}$  is  $10^9 M_{\odot}$ . This is limited by the mass resolution of our  $N$ -body simulation (see Sect. 2.1). We vary  $\text{Log}_{10}(\frac{M_{\min}}{M_{\odot}})$  between  $[9, 12]$ .

- Minimum mass of X-ray emitting halo ( $M_{\min,X}$ ): In addition to the UV emitting sources, GRIZZLY also includes heating and ionization from X-ray emitting sources, such as quasars and high-mass X-ray binaries, as not necessarily all halos hosting stellar sources also host X-ray sources. We assume no emission of X-ray photons from halos with mass less than  $M_{\min,X}$ , while all other halos host X-ray emitting sources. We vary  $\text{Log}_{10}(\frac{M_{\min,X}}{M_{\odot}})$  between  $[9, 12]$ .

- X-ray heating efficiency ( $f_X$ ): This scales the emission rate of X-ray photons per unit stellar mass from a halo as  $\dot{N}_X = f_X \times 10^{42} \text{ s}^{-1} M_{\odot}^{-1}$ . We model the spectrum of an X-ray source as a power-law of the energy  $E$ , i.e.  $I_X(E) \propto E^{-\alpha}$ , where we fix the

<sup>9</sup> Partnership for Advanced Computing in Europe: <http://www.prace-ri.eu/>

<sup>10</sup> The effects of RSD can enhance the large-scale power spectrum by a

factor of  $\approx 2$  in case it is driven by density fluctuations. In our case, we underestimate the power spectra values for those scenarios.

<sup>11</sup> <http://www2.iap.fr/pegase/>

**Table 2.** An overview of the IGM parameters considered in this paper. Note that the ‘heated region’ denotes the regions in the IGM with gas temperature larger than  $T_{\gamma, \text{eff}}$ .

IGM Parameters	Description
$\overline{x_{\text{HII}}}$	Volume averaged ionized fraction
$\overline{T_K}$ (K)	Volume averaged gas temperature in the partially ionized IGM with $x_{\text{HII}} < 0.5$
$\overline{\delta T_b}$ (mK)	Mass averaged differential brightness temperature
$f_{\text{heat}}$	Volume fraction of regions with temperature larger than $T_{\gamma, \text{eff}}$
$R_{\text{peak}}^{\text{heat}}$ (Mpc/h)	Size at which the PDF of the size distribution of the heated regions peaks
$\Delta R_{\text{FWHM}}^{\text{heat}}$ (Mpc/h)	FWHM of the PDF of the size distribution of the heated regions

spectral index  $\alpha$  to 1.2. The value of  $\dot{N}_X$  for  $f_X = 1$  is consistent with the measurements of high-mass X-ray binaries in local star forming galaxies in the 0.5-8 keV band (Mineo et al. 2012; Islam et al. 2019). We assume that the X-ray band spans from 100 eV to 10 keV. We vary  $\text{Log}_{10}(f_X)$  between  $[-3, 2]$ .

- **Radio background efficiency ( $A_r$ ):** This parameter quantifies the contribution of a potential radio background existing in addition to the CMB. For the LOFAR upper limits this parameter was not considered in Ghara et al. (2020) but was instead studied in a separate paper by Mondal et al. (2020). We model the effective brightness temperature of the radio background as (Fialkov & Barkana 2019; Mondal et al. 2020),

$$T_{\gamma, \text{eff}} = T_{\gamma} \left[ 1 + A_r \left( \frac{\nu_{\text{obs}}}{78 \text{ MHz}} \right)^{-2.6} \right], \quad (2)$$

where  $\nu_{\text{obs}}$  is the frequency of observation.  $T_{\gamma, \text{eff}}$  can differ from  $T_{\gamma}$  in presence of a radio background of any astrophysical or cosmological origin. Its existence is motivated by the evidence of an excess radio background above the CMB towards the Rayleigh-Jeans part of the spectrum, as detected by ARCADE2 (Fixsen et al. 2011) and LWA1 (Dowell & Taylor 2018). The LWA1 measurement of the excess radio background at frequency 40-80 MHz fits well with a power-law with spectral index  $-2.58 \pm 0.05$  with a temperature of  $603^{+102}_{-92}$  mK at 1.42 GHz. Varying  $T_{\gamma, \text{eff}}$  changes the brightness temperature maps although the ionization and gas temperature maps from GRIZZLY remain unchanged. We vary  $A_r$  from 0 to 416, where the lower bound stands for no excess radio background and the upper bound represents the upper limits of 0.603 K as measured by LWA1. Note that the radio background used in this study is uniform, while in general an inhomogeneous radio background may enhance the power spectrum even more than what we estimate here (Reis et al. 2020b). A study with inhomogeneous radio background is beyond the scope of this paper.

### 2.3 Derived IGM parameters

One should realise that the 21-cm signal observations do not contain any direct information about the properties of the sources at the redshift of interest. Instead, the 21-cm signal characterises the state of the IGM at those redshifts. Thus, the main focus of this study is on the IGM properties rather than on the source properties, i.e. we aim to constrain the physical properties of IGM, such as the ionization and thermal state, rather than the astrophysical simulation parameters used to simulate the brightness temperature maps. Below

we list the IGM parameters that we consider here at each redshift (see also in Table 2):

- $\overline{x_{\text{HII}}}$ : Volume averaged ionized fraction of the IGM.
- $\overline{T_K}$  (K): Volume averaged gas temperature of the regions in the IGM with ionization fraction  $x_{\text{HII}} < 0.5$ .
- $\overline{\delta T_b}$  (mK): Mass averaged differential brightness temperature in the IGM.
- $f_{\text{heat}}$ : Volume fraction of the IGM with gas temperature  $T_K > T_{\gamma, \text{eff}}$ .
- $R_{\text{peak}}^{\text{heat}}$  (cMpc): Size of the ‘heated regions’, i.e. regions with  $T_K > T_{\gamma, \text{eff}}$  at which the probability distribution function (PDF) of the sizes peaks. To determine the size distribution of the heated regions we use the mean free path (MFP) method, which is a Monte Carlo based approach (Mesinger & Furlanetto 2007; Giri et al. 2018a).
- $\Delta R_{\text{FWHM}}^{\text{heat}}$  (cMpc): Full width at half maximum (FWHM) of the PDF of the sizes of the heated regions.

Unlike in Ghara et al. (2020), here we have not considered separate IGM parameters for the H II regions. In the absence of X-ray heating, the ‘heated regions’ in the IGM are equivalent to the H II regions, as the kinetic temperature of the gas within such regions is  $\sim 10^4$  K. Thus, for insignificant heating in the neutral IGM,  $f_{\text{heat}}$  is equivalent to  $\overline{x_{\text{HII}}}$ , while  $R_{\text{peak}}^{\text{heat}}$  and  $\Delta R_{\text{FWHM}}^{\text{heat}}$  characterise the size distribution of the H II regions. Note that we estimate these quantities from GRIZZLY simulations at our simulation resolution.

### 2.4 Bayesian inference framework

We generate  $10^5$  power spectra and sets of IGM parameters at each redshift point using GRIZZLY, while employing the gridded sampling method to sample the 5D parameter space. We then use a linear interpolation scheme<sup>12</sup> on a regular grid to determine the power spectrum for a set of parameters  $\theta$ . To avoid extrapolation, the range of  $\theta$  used is the same as the range of the gridded parameter space covered by the GRIZZLY simulations performed for this study. We use the regular grid interpolation method implemented in SCIPY python package (Weiser & Zarantonello 1988; Virtanen et al. 2020). See Monsalve et al. (2018) for a similar Bayesian framework that is based on interpolation in a regular grid of 4D parameter space. This linear interpolator is used in the EMCEE python MCMC module (Foreman-Mackey et al. 2013) to explore the parameter space as described in section 2.2. Note that we use only the smallest three  $k$ -bin values from Trott et al. (2020), i.e. 0.142, 0.212 and 0.283  $h \text{ Mpc}^{-1}$ , as the upper limits at other wavenumbers are too high to give any additional constraints.

The MCMC analysis requires the calculation of a likelihood. As we are working with upper limits we cannot use the formal  $\chi^2$  which only applies for actual measurements of a signal. Also, as the upper limits have quite high values, we want our framework to find the models which are excluded, rather than the ones which are allowed. Given a measured upper limit of the power spectrum at redshift  $z$  as  $\Delta_{21}^2(k_i, z) \pm \Delta_{21, \text{err}}^2(k_i, z)$ , the likelihood of a set of

<sup>12</sup> Note that in our previous study (Ghara et al. 2020) we used an emulator based on the Gaussian Process Regression (GPR) algorithm. However, GPR does not scale well with the size of the training set (e.g. Rasmussen & Williams 2006). As the parameter space used here has a higher dimension than the one explored in Ghara et al. (2020), a larger training set is needed. Tests showed that this would lead the emulator to achieve a size of several tens of gigabytes, slowing it down too much to be useful.



**Table 3.** The  $\Delta_{\text{up}}^2 \equiv \Delta_{21}^2 + 2\sigma_{21,\text{err}}$  upper limits from MWA observations at different redshifts for different  $k$ -bins. See Trott et al. (2020) for details. We obtained  $\Delta_{21}^2$  and the corresponding error from private communication with the MWA team.

$k$ ( $h \text{ Mpc}^{-1}$ )	$\Delta_{\text{up}}^2(k)$ ( $\text{mK}^2$ ) at $z=6.5$	$\Delta_{\text{up}}^2(k)$ ( $\text{mK}^2$ ) at $z=6.8$	$\Delta_{\text{up}}^2(k)$ ( $\text{mK}^2$ ) at $z=7.1$	$\Delta_{\text{up}}^2(k)$ ( $\text{mK}^2$ ) at $z=7.8$	$\Delta_{\text{up}}^2(k)$ ( $\text{mK}^2$ ) at $z=8.2$	$\Delta_{\text{up}}^2(k)$ ( $\text{mK}^2$ ) at $z=8.7$
0.142	43.1 <sup>2</sup>	60.1 <sup>2</sup>	77.7 <sup>2</sup>	154.2 <sup>2</sup>	167.7 <sup>2</sup>	249.6 <sup>2</sup>
0.212	70.2 <sup>2</sup>	90.0 <sup>2</sup>	117.4 <sup>2</sup>	247.5 <sup>2</sup>	430.3 <sup>2</sup>	569.9 <sup>2</sup>
0.283	93.3 <sup>2</sup>	114.1 <sup>2</sup>	152.3 <sup>2</sup>	314.5 <sup>2</sup>	422.2 <sup>2</sup>	562.5 <sup>2</sup>
0.354	209.5 <sup>2</sup>	243.9 <sup>2</sup>	281.5 <sup>2</sup>	460.1 <sup>2</sup>	540.9 <sup>2</sup>	688.1 <sup>2</sup>
0.425	183.5 <sup>2</sup>	221.3 <sup>2</sup>	263.3 <sup>2</sup>	804.4 <sup>2</sup>	772.8 <sup>2</sup>	963.2 <sup>2</sup>
0.495	125.5 <sup>2</sup>	169.0 <sup>2</sup>	231.9 <sup>2</sup>	466.8 <sup>2</sup>	1402.6 <sup>2</sup>	1854.5 <sup>2</sup>
0.566	210.1 <sup>2</sup>	255.4 <sup>2</sup>	310.9 <sup>2</sup>	484.4 <sup>2</sup>	1109.9 <sup>2</sup>	1546.0 <sup>2</sup>
0.637	214.1 <sup>2</sup>	260.3 <sup>2</sup>	333.8 <sup>2</sup>	501.0 <sup>2</sup>	739.1 <sup>2</sup>	962.3 <sup>2</sup>
0.708	384.6 <sup>2</sup>	383.1 <sup>2</sup>	437.9 <sup>2</sup>	613.4 <sup>2</sup>	781.1 <sup>2</sup>	947.6 <sup>2</sup>

parameters  $\theta$  to be excluded is defined as (see Ghara et al. 2020, for details)

$$\mathcal{L}_{\text{ex}}(\theta, z) = 1 - \prod_i \frac{1}{2} \left[ 1 + \text{erf} \left( \frac{\Delta_{21}^2(k_i, z) - \Delta_{\text{m}}^2(k_i, \theta, z)}{\sqrt{2}\sigma(k_i, z)} \right) \right], \quad (3)$$

where  $k_i$  denotes the 3  $k$ -bins of the measured power spectrum, and  $\Delta_{\text{m}}^2(k, \theta, z)$  the model power spectrum for a set of parameters  $\theta$  for  $k$ -scale at redshift  $z$ . The quantity  $\sigma$  accounts for errors from the measurement, as well as the modelling error, i.e.  $\sigma^2 = \Delta_{21,\text{err}}^4 + \Delta_{\text{m},\text{err}}^4$ . We adopt 30 per cent modelling error  $\Delta_{\text{m},\text{err}}^2(k_i, z) = 0.3 \times \Delta_{\text{m}}^2(k_i, \theta, z)$  to incorporate errors from the modelling with the code GRIZZLY and from the interpolation scheme. In Ghara et al. (2018) we performed a detailed comparison of GRIZZLY with the 3D radiative transfer scheme C<sup>2</sup>RAY, and found that the error from GRIZZLY is less than 10 per cent. We estimate the error due to the interpolation scheme on a test set of the power spectra and found it to be less than 30 per cent for the scales of interest. Note that the sample variances on the power spectrum at the scales of interest are negligible compared to the adopted modelling errors.

Unlike Greig et al. (2021a), we consider the upper limits at each redshift independently to obtain constraints on the simulation parameters and thereafter on the IGM parameters. One requires a background source model to derive constraints on the simulation parameters using multi-redshift constraints. Thus, the derived constraints on the IGM parameters at individual redshifts from such a combined upper limits analysis would be source model dependent. Moreover, those constraints would be biased as the likelihood in that case would be mostly dominated by the best upper limit at  $z \approx 6.5$  (see Table 3). Thus, to avoid dependence of the quantities of our interest on the background source model, we consider the upper limits at each redshift independently.

Once the MCMC chains that contain the lists of the simulation parameters used in the MCMC analysis is built, we generate the list of corresponding IGM parameters using the interpolation scheme. Finally, these are used to determine the posterior distribution of the IGM parameters.

### 3 RESULTS

In this section, we apply the Bayesian inference framework described in the previous section to the measured upper limits from

Trott et al. (2020). These  $2\sigma$  upper limits are also shown in Table 3. Clearly, the upper limits are stronger at the larger (spatial) scales (lower ‘ $k$ ’ values) and lower redshifts. Figure 1 shows the set of the power spectra generated with GRIZZLY for  $A_r = 0$  at redshift 6.5 (left panel) and 7.8 (right panel), respectively. The red points in the panels denote the measured MWA  $2\sigma$  upper limits on the power spectrum. Clearly, the power spectrum amplitude of a significant fraction of the models is above the upper limit at scales  $\lesssim 0.2 h \text{ Mpc}^{-1}$  at  $z = 6.5$ , even in the absence of an excess radio background. This is also true for redshifts 6.8 and 7.2. On the other hand, the right panel shows that the upper limits at  $z = 7.8$  (and also for  $z = 8.2$  and  $8.7$ ) remain above the power spectra values from GRIZZLY for  $A_r = 0$ .

As explained in Section 2.4 the MCMC provides the probability of the models to be excluded by the MWA upper limits. Each MCMC run consists of 10 walkers and  $10^6$  steps. We find that the MCMC chains converge well before the final step. The explored parameters ranges are listed in Table 1. Note that all the priors are flat or uniform in log-scale.

To constrain the IGM parameters using our inference framework we consider a case with  $A_r = 0$ , i.e. no excess radio background contribution to the CMB, and one in which we also vary the  $A_r$  parameter. We will first explore the scenario without any excess radio background in Section 3.1, while in Section 3.2 we present the constraints allowing  $A_r$  parameter to vary.

#### 3.1 Analysis without excess radio background

First, we explore the four-dimensional source parameter space, i.e.  $\zeta$ ,  $M_{\text{min}}$ ,  $M_{\text{min},X}$  and  $f_X$ , using MCMC at six different redshifts. We fix  $A_r = 0$ , i.e. we initially assume that the radio background is contributed by the CMB alone.

The posterior distribution of the source parameter space of the excluded models at  $z = 6.5$ , our fiducial redshift, is shown in Figure 2. Three main scenarios can be envisioned that produce a high amplitude of the large-scale power spectrum. In the first scenario the large-scale power spectrum is dominated by  $x_{\text{HII}}$  fluctuations, which are enhanced by a distribution of rare but large H II regions in the IGM. Note that the large-scale power-spectrum decreases for a highly ionized IGM with  $\bar{x}_{\text{HII}} \gtrsim 0.5$ , and almost vanishes for  $\bar{x}_{\text{HII}} \sim 1$ . This suggests that high values of  $\zeta$  and low values of  $M_{\text{min}}$  should be disfavored among the excluded models, as confirmed

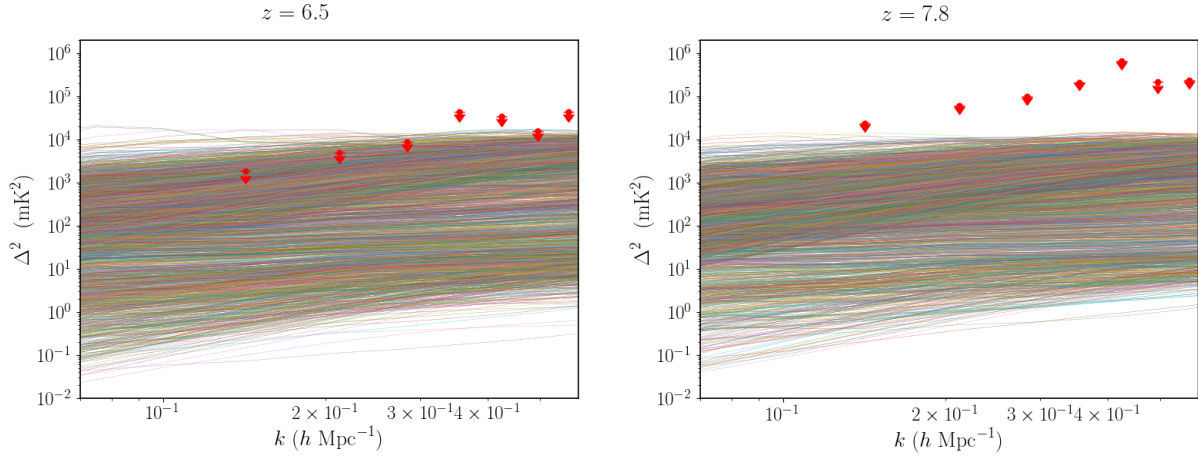


**Figure 1.** A subset of the power spectra of the 21-cm signal brightness temperature generated using GRIZZLY over the gridded parameter space. These correspond to  $A_r = 0$  or, equivalently,  $T_{\gamma, \text{eff}} = 2.725 \times (1 + z)$  K. Note that we have varied  $A_r$  to get the full power spectra set. Left and right panels correspond to  $z \approx 6.5$  and  $z \approx 7.8$ , respectively. The red points refer to the recent MWA  $2\sigma$  upper limits from Trott et al. (2020).

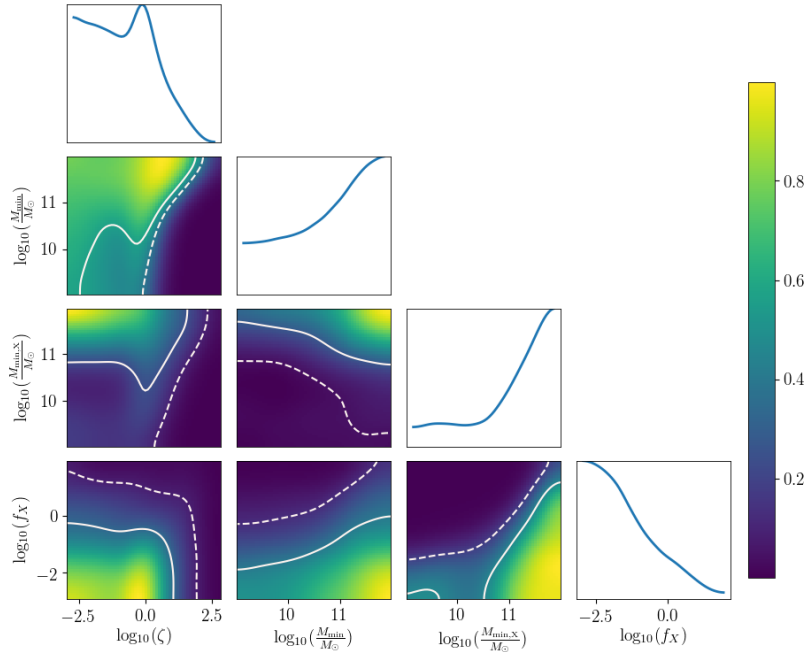


**Figure 2.** Posterior distribution of the simulation parameters at  $z \approx 6.5$  from the MCMC analysis. Here  $A_r = 0$ . The color-bar shows the marginalized probability of the models to be ruled out. The solid and dashed curves corresponds to the 68 and 95 per cent credible intervals of the models ruled out by the MWA upper limit at that redshift. The diagonal panels refer to the marginalized probability distributions for ruled out simulation parameters.

in the figure. From this, we deduce that  $\zeta \lesssim 2.4$  and  $M_{\min} \gtrsim 3 \times 10^{10} M_{\odot}$  are the most likely to be excluded within the 68 per cent credible intervals by the MWA upper limit at redshift 6.5 alone. Note also that a colder IGM, which is obtained with a smaller value of  $f_X$ , will also enhance the large-scale power spectrum in this scenario. An alternative scenario that produces a high amplitude of the large-scale power spectrum is when the latter is dominated by  $T_S/T_K$  fluctuations. This scenario can happen for a small number density of X-ray emitting sources, as numerous X-ray sources and high X-ray emissivity can easily heat the IGM above  $T_{\gamma}$

and suppress the large-scale power spectrum. Indeed,  $f_X \lesssim 0.1$  and  $M_{\min, X} \gtrsim 10^{11} M_{\odot}$  are the most likely to be excluded within the 68 per cent credible intervals by the MWA upper limit at redshift 6.5 alone. Alternatively, a scenario with neutral and cold IGM (as indicated by low values of  $\zeta$  and  $f_X$ ) where the large-scale power spectrum is dominated mainly by the density fluctuations is also important.

While the parameters the  $M_{\min}$ ,  $M_{\min, X}$  and  $f_X$  show a smooth distribution over the explored ranges, one can see a distinct peak around  $\zeta \approx 1$  in the posterior distribution of  $\zeta$  in Figure 2. The

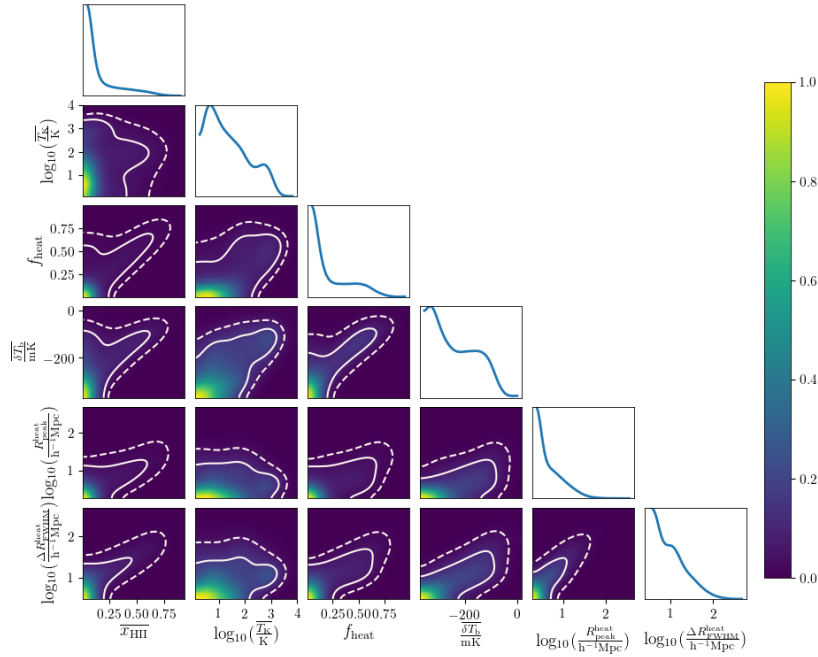


**Figure 3.** Posterior distribution of the IGM parameters at  $z \approx 6.5$  from the MCMC analysis. Here  $A_r = 0$ . The color-bar shows the marginalized probability of the models to be ruled out. The solid and dashed curves corresponds to the 68 and 95 per cent credible intervals of the models ruled out by the MWA upper limit at that redshift. The diagonal panels refer to the marginalized probability distributions for ruled out IGM parameters.

**Table 4.** Constraints on the excluded part of the IGM parameter space at different redshifts for the scenario where  $A_r = 0$ , i.e. no excess radio background is considered in addition to the CMB. These are obtained from the MCMC analysis using the multi-redshift MWA upper limits from [Trott et al. \(2020\)](#). The priors are derived from the GRIZZLY simulations.

IGM Parameters	Credible intervals	$z = 6.5$	$z = 6.8$	$z = 7.2$
$\bar{x}_{\text{HII}}$	Prior	[0, 1]	[0, 1]	[0, 1]
	68%	[0, 0.15]	[0, 0.15]	[0, 0.26]
	95%	[0, 0.56]	[0, 0.53]	[0, 0.56]
$\bar{T}_K$ (K)	Prior	[1.17, $10^4$ ]	[1.28, $10^4$ ]	[1.38, $10^4$ ]
	68%	[1.17, 40.1]	[1.28, 11]	[1.38, 15.7]
	95%	[1.17, 251]	[1.28, 158]	[1.38, 90]
$f_{\text{heat}}$	Prior	[0, 1]	[0, 1]	[0, 1]
	68%	[0, 0.28]	[0, 0.18]	[0, 0.28]
	95%	[0, 0.63]	[0, 0.55]	[0, 0.58]
$\delta \bar{T}_b$ (mK)	Prior	[-376, 23.3]	[-367, 23.8]	[-360, 24.4]
	68%	[-376, -140]	[-367, -247]	[-360, -229]
	95%	[-376., -89]	[-367, -125]	[-360, -121]
$R_{\text{peak}}^{\text{heat}}$ ( $h^{-1}$ Mpc)	Prior	[0, 198]	[0, 203]	[0, 201]
	68%	[0, 4.7]	[0, 8.5]	[0, 18.2]
	95%	[0, 18.]	[0, 17.5]	[0, 30]
$\Delta R_{\text{FWHM}}^{\text{heat}}$ ( $h^{-1}$ Mpc)	Prior	[0, 440]	[0, 445]	[0, 452]
	68%	[0, 12.5]	[0, 16.6]	[0, 35]
	95%	[0, 47]	[0, 39]	[0, 63]

combination of  $\zeta \approx 1$  and a high value of  $M_{\text{min}} \gtrsim 10^{11} M_{\odot}$  maximises the contribution from ionisation fluctuations. These ionization states correspond to  $\bar{x}_{\text{HII}} \sim 0.5$ . On the other hand, the other two scenarios, i.e. density fluctuations in a cold and neutral IGM and  $T_S$  fluctuations in a neutral IGM, maximise the PDF for  $\bar{x}_{\text{HII}} \sim 0$ , which requires small values for  $\zeta$ . This bimodal feature in the PDF of  $\zeta$  is consistent with the results of [Ghara et al. \(2020\)](#), where we perform a similar analysis for LOFAR upper limits at redshift 9.1. Note that we considered a prior on the ionization fraction at redshift 9.1 in [Ghara et al. \(2020\)](#).

Figure 3 shows the posterior distributions of the IGM parameters at redshift 6.5. The constraints on such parameters are also listed in Table 4. We find that an IGM with  $\bar{x}_{\text{HII}} \lesssim 0.56$ ,  $\bar{T}_K \lesssim 250$  K,  $f_{\text{heat}} \lesssim 0.63$ ,  $R_{\text{peak}}^{\text{heat}} \lesssim 18 h^{-1}$  Mpc and  $\Delta R_{\text{FWHM}}^{\text{heat}} \lesssim 50 h^{-1}$  Mpc falls within 95 per cent credible intervals of the ruled out IGM scenarios. The same limit for the average brightness temperature is  $\delta \bar{T}_b \lesssim -90$  mK. The PDFs of  $\bar{x}_{\text{HII}}$ ,  $f_{\text{heat}}$  and  $\delta \bar{T}_b$  suggest that the set of excluded models contains a significant number of models in which the IGM is still neutral and cold at redshift  $z \approx 6.5$ . A similar conclusion was reached by [Greig et al. \(2021a\)](#). However, it is hard to tell from the achieved limits on the IGM parameters if these neutral models are completely cold or contain patchy heated regions in an otherwise cold IGM.

The 68 and 95 per cent credible intervals limits of the excluded IGM parameters for other redshifts are also listed in Table 4. As the upper limit of the power spectrum from MWA is weaker at a higher redshift, the limits also become weaker, and especially for  $z \gtrsim 7.8$  their significance is very small. In fact, we neither get any constraint on the source nor on the IGM parameters at  $z \approx 8.7$ . For  $z \approx 7.8$  and 8.2, the values of  $\log_{10}(\mathcal{L}_{\text{ex}})$  remain  $\lesssim -5$ , which corresponds to the value of  $\log_{10}(\mathcal{L}_{\text{ex}})$  when a modelled power spectrum is below

**Table 5.** Constraints on the excluded part of the IGM parameter space at different redshifts for a varying radio background scenario. These are obtained from the MCMC analysis using the multi-redshift upper limits from MWA (Trott et al. 2020). The priors are derived from the simulations run with GRIZZLY.

IGM Parameters	Credible intervals	$z = 6.5$	$z = 6.8$	$z = 7.2$	$z = 7.8$	$z = 8.2$	$z = 8.7$
$\text{Log}_{10}(A_r)$	Prior	[-2, 2.6 ]	[-2, 2.6 ]	[-2, 2.6 ]	[-2, 2.6 ]	[-2, 2.6 ]	[-2, 2.6 ]
	68%	[0.4, 2.6 ]	[1, 2.6 ]	[1.4, 2.6 ]	[1.87, 2.6 ]	[1.88, 2.6 ]	[1.9, 2.6 ]
	95%	[-0.8, 2.6 ]	[-0.76, 2.6 ]	[-0.65, 2.6 ]	[1.36, 2.6 ]	[1.38, 2.6 ]	[1.43, 2.6 ]
$\overline{x_{\text{HII}}}$	Prior	[0, 1]	[0, 1]	[0, 1]	[0, 1]	[0, 1]	[0, 1]
	68%	[0, 0.15]	[0, 0.15]	[0, 0.17]	[0, 0.12]	[0, 0.15]	[0, 0.12]
	95%	[0, 0.58]	[0, 0.53]	[0, 0.56]	[0, 0.56]	[0, 0.55]	[0, 0.52]
$\overline{T_K}$ (K)	Prior	[1.17, $10^4$ ]	[1.28, $10^4$ ]	[1.38, $10^4$ ]	[1.63, $10^4$ ]	[1.75, $10^4$ ]	[2, $10^4$ ]
	68%	[1.17, 208]	[1.28, 80.7]	[1.38, 69]	[1.63, 69]	[1.75, 68]	[2, 42]
	95%	[1.17, 1025]	[1.28, 795]	[1.38, 790]	[1.63, 602]	[1.75, 592]	[2, 400.]
$f_{\text{heat}}$	Prior	[0, 1]	[0, 1]	[0, 1]	[0, 1]	[0, 1]	[0, 1]
	68%	[0, 0.33]	[0, 0.28]	[0, 0.28]	[0, 0.28]	[0, 0.23]	[0, 0.18]
	95%	[0, 0.64]	[0, 0.6]	[0, 0.59]	[0, 0.56]	[0, 0.57]	[0, 0.55]
$\text{Log}_{10}(\frac{ \delta T_b }{\text{mK}})$	Prior	[1.37, 4.6]	[1.38, 4.59]	[1.39, 4.58]	[1.4, 4.57]	[1.41, 4.56]	[1.43, 4.54]
	68%	[2.18, 3.3]	[2.4, 3.57]	[2.65, 3.76]	[3.21, 4]	[3.24, 4.04]	[3.38, 4.06]
	95%	[1.96, 4.2]	[2.18, 4.24]	[2.29, 4.27]	[2.94, 4.39]	[2.98, 4.38]	[3.19, 4.43]
$R_{\text{peak}}^{\text{heat}}$ ( $h^{-1}\text{Mpc}$ )	Prior	[0, 198]	[0, 203]	[0, 201]	[0, 201]	[0, 216]	[0, 198]
	68%	[0, 4.]	[0, 3.3]	[0, 3]	[0, 3.6]	[0, 3.6]	[0, 3.5]
	95%	[0, 12.]	[0, 10]	[0, 13]	[0, 12]	[0, 11.5]	[0, 11.5]
$\Delta R_{\text{FWHM}}^{\text{heat}}$ ( $h^{-1}\text{Mpc}$ )	Prior	[0, 440]	[0, 445]	[0, 452]	[0, 452]	[0, 447]	[0, 452]
	68%	[0, 14]	[0, 9.1]	[0, 11.4]	[0, 10.]	[0, 11.2]	[0, 9.3]
	95%	[0, 29]	[0, 22]	[0, 26]	[0, 23]	[0, 25]	[0, 23]

$3\sigma$  error of the observed upper limits at all three scales. Clearly, the reason is that all the GRIZZLY models have power spectra values that are well below the upper limits (see Figure 1). As the significance of the limits at redshifts  $\geq 7.8$  is poor, we do not show them in this work. Note that the limits as stated in Table 4 only stand for the part of the parameter space which has the largest probability to be ruled out.

### 3.2 Analysis with varying radio background

Now, we explore the five-dimensional simulation parameter space, i.e.  $\zeta$ ,  $M_{\text{min}}$ ,  $M_{\text{min},X}$ ,  $f_X$  and  $A_r$  using MCMC at six different redshifts. The explored ranges of the simulation parameters are listed in Table 1.

Figure 4 shows the posterior distribution of the simulation parameters of the models with high exclusion probability at  $z \approx 6.5$ . The 68 per cent credible intervals limits of these model parameters are  $\zeta \lesssim 1$ ,  $M_{\text{min}} \gtrsim 2 \times 10^{10} M_{\odot}$ ,  $M_{\text{min},X} \gtrsim 4 \times 10^{10} M_{\odot}$  and  $f_X \lesssim 0.1$ . As the amplitude of the power spectrum increases with increasing  $A_r$ , the excluded models prefer a higher value of  $A_r$ .

From this five-dimensional MCMC analysis, in fact, we find that  $A_r \gtrsim 0.15$  ( $\gtrsim 2.5$ ) is the most likely to be excluded within the 95 (68) per cent credible intervals by the MWA upper limit at redshift 6.5 alone.

Figure 5 shows instead the posterior distributions of the IGM parameters at the same redshift. These constraints are also listed in Table 5 and show that an IGM with  $\overline{x_{\text{HII}}} \lesssim 0.6$ ,  $\overline{T_K} \lesssim 10^3$  K,  $f_{\text{heat}} \lesssim 0.65$ ,  $R_{\text{peak}}^{\text{heat}} \lesssim 13 h^{-1} \text{Mpc}$  and  $\Delta R_{\text{FWHM}}^{\text{heat}} \lesssim 30 h^{-1} \text{Mpc}$  falls within 95 per cent credible intervals of the ruled out IGM scenarios. As these intervals indicate a larger value of  $A_r$  (i.e.  $A_r \gtrsim 2.5$ ), the derived limit of the average brightness temperature,  $\overline{\delta T_b} \gtrsim -10^4 \text{mK}$ , is weaker compared to what we had found for  $A_r = 0$ .

The constraints on the IGM parameters for the other five redshifts are also listed in Table 5 and presented in Fig. 6. We find that the 95 per cent credible intervals for each of the quantities,  $\overline{x_{\text{HII}}}$ ,  $f_{\text{heat}}$ ,  $R_{\text{peak}}^{\text{heat}}$  and  $\Delta R_{\text{FWHM}}^{\text{heat}}$ , are similar at all six redshifts. This shows that the ionization and thermal states of the IGM which are given by the IGM parameter values within these limits produce



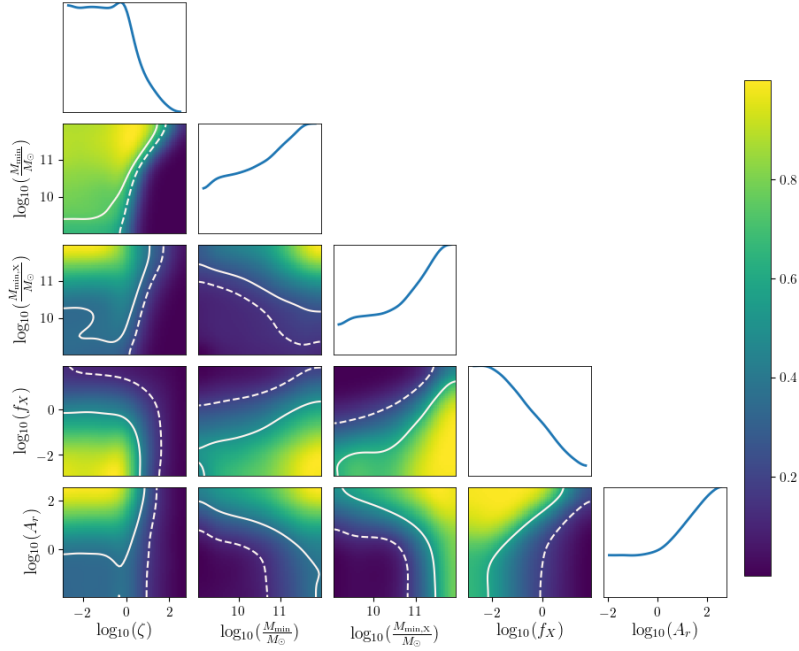


**Figure 4.** Posterior distribution of the simulation parameters at  $z \approx 6.5$  from the MCMC analysis. The color-bar shows the marginalized probability of the models to be ruled out. The solid and dashed curves corresponds to the 68 and 95 per cent credible intervals of the models ruled out by the MWA upper limit at that redshift. The diagonal panels refer to the marginalized probability distributions for ruled out simulation parameters.

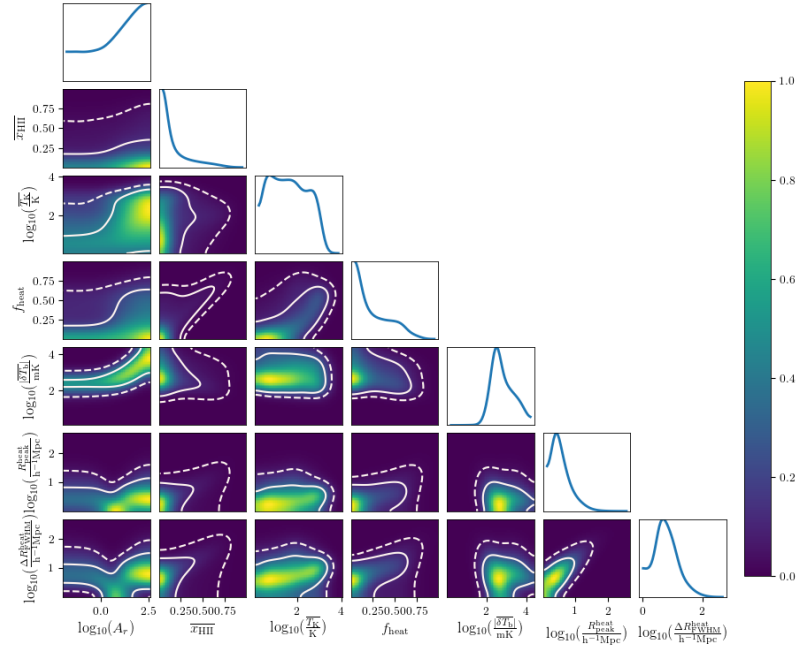


**Figure 5.** Posterior distribution of the IGM parameters at  $z \approx 6.5$  from the MCMC analysis. The color-bar shows the marginalized probability of the models to be ruled out. The solid and dashed curves corresponds to the 68 and 95 per cent credible intervals of the models ruled out by the MWA upper limit at that redshift. The diagonal panels refer to the marginalized probability distributions for ruled out IGM parameters. Note that we have used Logarithm of the absolute values of  $\overline{\delta T_b}$  as the range is large. In reality,  $\overline{\delta T_b}$  values of these excluded models are mostly negative.

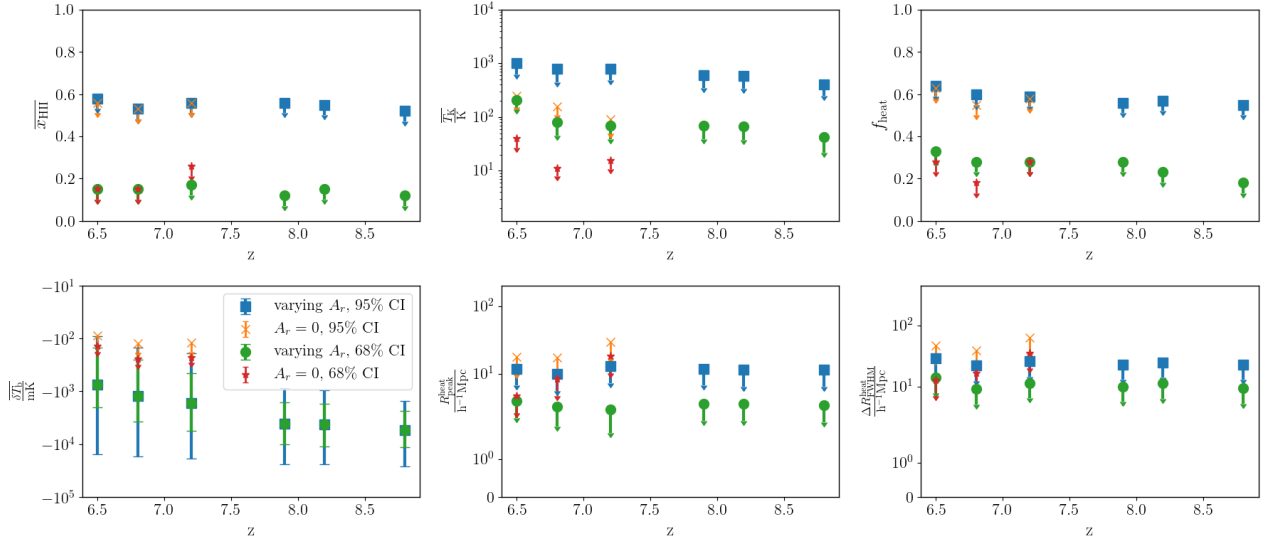


**Figure 6.** limits on the IGM parameters as obtained from the excluded models at six different redshifts using the recent MWA upper limits within 68 and 95 per cent credible interval. These constraints have been determined at each redshift independently. For  $z \geq 7.8$ , no constraints are found in absence of an additional radio background ( $A_r = 0$ ).

extreme amplitudes of the large-scale power spectra, while the limits on the IGM parameters are independent of redshift. Note that because the source populations differ between redshifts, it will require different values of the source parameters to achieve similar thermal and ionization state of the IGM at different redshifts. As the power spectrum amplitude increases with increasing  $A_r$  and the upper limits are weaker at higher  $z$ , the 95 per cent credible interval limit for  $A_r$  increases as well, for example from  $\approx 0.15$  at redshift 6.5 to  $\approx 27$  at redshift 8.7. These correspond to  $T_{\gamma, \text{eff}} \approx 26$  K and 140 K at redshifts 6.5 and 8.7, respectively. The limit at redshift 6.5 is equivalent to an excess radio background which is 0.008% of the CMB at 1.42 GHz. Excess of 0.009%, 0.01%, 1.2%, 1.3% and 1.5% are found from the limits at redshifts 6.8, 7.2, 7.8, 8.2 and 8.7, respectively.

#### 4 DISCUSSION

We highlight that the constraints on the IGM and the simulation parameters obtained in the previous section do not correspond to models ruled out with a high significance, but rather to models that have a high probability to be excluded. Future stronger upper limits will improve the significance/probability of the models to be ruled out.

It should be noted that the part of the parameter space which has high probability to be excluded is associated with models that produce a high amplitude of the large-scale power spectrum. Large ionized regions in a cold IGM, and/or large heated regions in a non-uniform spin temperature IGM are the obvious scenarios that come to mind. Alternatively, density fluctuations in a cold IGM can also produce high values of the large-scale power spectrum, especially at the lower redshifts where the density fluctuations are larger and the IGM is expected to be colder in the absence of heating sources. The same models also suggest a high amplitude of the excess radio background, as this boosts the fluctuations at all scales. It is challenging to devise scenarios alternative to those discussed here that have such a high chance of exclusion without

accounting for other non-standard physics, such as e.g. an excess cooling mechanism that makes the gas in the IGM colder than in a standard scenario.

As we consider each redshift independently, the models more likely to be excluded show similar IGM conditions (e.g.  $\bar{x}_{\text{HI}} \lesssim 0.5$  and cold IGM) at all redshifts, although the constraints become obviously stronger at redshifts with tighter upper limits. In our previous study (Ghara et al. 2020), we obtained constraints on the IGM parameters at  $z \approx 9.1$  using the upper limits from LOFAR (Mertens et al. 2020), finding that an IGM with  $f_{\text{heat}} \lesssim 0.35$ ,  $T_K \lesssim 160$  K,  $R_{\text{peak}}^{\text{heat}} \lesssim 70 h^{-1} \text{Mpc}$  and  $\Delta R_{\text{FWHM}}^{\text{heat}} \lesssim 110 h^{-1} \text{Mpc}$  is the most likely to be ruled out within 95 per cent credible interval limits. This physical state of the IGM is similar to those found to be more likely ruled out in the present study. This is to be expected, as those states of the IGM which produce high amplitudes of the large-scale power spectra are easy to exclude by the 21-cm signal upper limits.

We note that, for some of the models with high exclusion probability, the large-scale power spectrum is driven by  $T_S$  fluctuations (and/or density fluctuations) only when the  $x_{\text{HI}}$  fluctuations are small. These models have an ionization fraction  $\bar{x}_{\text{HI}} \approx 0$  at  $z \approx 6.5$ , which is inconsistent with the combined constraints from observations of the Thomson scattering optical depth and  $z > 6$  quasar spectra (see e.g., Mitra et al. 2015), as well as Ly $\alpha$  emitter statistics (Ouchi et al. 2010), spectroscopy of gamma-ray bursts (Chornock et al. 2013), dark pixel statistics of the spectroscopy of high- $z$  quasars (McGreer et al. 2015), which all indicate that the IGM is not highly neutral at redshift  $\lesssim 7$ .

The constraints presented in the previous section are obtained analysing only one of the six upper limits/redshifts at a time. In the MCMC analysis the upper limits are not all combined into a single likelihood, as otherwise this would be mostly driven by the best upper limit, i.e. the one at  $z \approx 6.5$ , biasing the conclusions on the IGM properties at individual redshifts.

A recent study by Greig et al. (2021a) obtained constraints on source parameters using the MWA upper limits by combining all

redshifts into a single likelihood for a set of redshift independent source parameters. The derived constraints on the IGM parameters at different redshifts as obtained in fig 6 of Greig et al. (2021a) depend on the background source model. As a result, the constraints on  $\overline{x_{\text{HII}}}$  follow a redshift evolution as expected in such model. We on the other hand constrain the IGM state at each redshift using the upper limits of the power spectra at that redshift only, and thus the constraints do not depend on the redshift evolution in the background model. The differences in the analysis methods make it hard to directly compare our results with those in Greig et al. (2021a). However, as the results of Greig et al. (2021a) are expected to be biased by the strongest upper limits at redshift 6.5, one might expect that the IGM states of the excluded models of both studies are qualitatively similar at redshift 6.5, which we indeed have found to be the case in Section 3.1.

Using LOFAR upper limits at  $z = 9.1$  from Mertens et al. (2020), Mondal et al. (2020) obtained constraints on the excess radio background as 0.1 – 9.6% of the CMB at 1.42 GHz. Note that these 95 per cent credible limits are obtained from marginalizing models *which are valid* under the LOFAR upper limits. Our limits are instead derived from the marginalization of the *excluded models*. It is therefore not possible to compare the above constraint to the one we find, namely that the 95 per cent credible limits of  $A_r$  at redshift 8.7 (6.5) correspond to an excess radio background which is 1.5% (0.008%) of the CMB at 1.42 GHz.

## 5 SUMMARY & CONCLUSIONS

Trott et al. (2020) has provided new upper limits on the dimensionless spherically averaged power spectrum of the 21-cm signal from MWA at six different redshifts, in the range 6.5 – 8.7. The best  $2\sigma$  upper limit from that paper, obtained from 110 hours of integration time, is  $\Delta^2(k = 0.14 h \text{ Mpc}^{-1}) = (43)^2 \text{ mK}^2$  at  $z \approx 6.5$ . Here we have used these limits to rule out possible reionization scenarios. The main focus of this study is to constrain the ionization and thermal states of the IGM.

We use the GRIZZLY code to generate hundred of thousands of models for different combinations of parameters, namely, ionization efficiency ( $\zeta$ ), minimum mass of the UV emitting halos ( $M_{\text{min}}$ ), minimum mass of X-ray emitting halos ( $M_{\text{min,X}}$ ), X-ray heating efficiency ( $f_X$ ) and excess radio background efficiency ( $A_r$ ). The outputs of these models are power spectra and derived IGM parameters, such as volume averaged ionization fraction ( $\overline{x_{\text{HII}}}$ ), volume averaged gas temperature of the partially ionized IGM ( $\overline{T_K}$ ), mass averaged brightness temperature ( $\overline{\delta T_b}$ ), volume fraction of the heated region ( $f_{\text{heat}}$ ), size of the heated regions at which the PDF of the sizes peaks ( $R_{\text{peak}}^{\text{heat}}$ ) and the FWHM of the PDFs ( $\Delta R_{\text{FWHM}}^{\text{heat}}$ ). The outputs from the GRIZZLY simulations are used within an MCMC framework to constrain the simulation parameters using the upper limits from MWA. The simulation parameters from the MCMC chains are later used to generate lists of IGM parameters. The main findings of the paper are the followings.

- From the set of power spectra generated using GRIZZLY, we do not find any model which can be excluded in the absence of an extra radio background component at redshifts 7.8, 8.2 and 8.7. On the other hand, we find a significant number of models that can be ruled out at the other three redshifts.
- From the MCMC analysis, we find that the excluded models are more likely to have a smaller number density of the UV as well as X-ray emitting sources. At redshift  $\approx 6.5$ , for 68 per cent credible

region of the excluded models, the mass of the dark matter halo that hosts these sources is  $\gtrsim 3 \times 10^{10} M_{\odot}$ , while  $\zeta \lesssim 1.4$  and  $f_X \lesssim 0.1$ .

- The probability with which a reionization model can be excluded increases with increasing  $A_r$ . We found  $A_r \gtrsim 0.15$  for the 95 per cent credibility interval of the excluded models at redshift 6.8. This limit increases for higher redshifts as the upper limits are weaker there. At the highest redshift of  $z = 8.7$  we find  $A_r \gtrsim 27$  for the same credibility interval. Within 95 per cent credible interval limits, the additional radio background is at least 0.008%, 0.009%, 0.01%, 1.2%, 1.3% and 1.5% of the CMB at 1.42 GHz at redshifts 6.5, 6.8, 7.2, 7.8, 8.2 and 8.7 respectively. These values differ with redshifts because the upper limits have been considered individually. In the presence of such radio background, the limits on the IGM parameters for the 95 per cent credible interval of the excluded models are  $\overline{x_{\text{HII}}} \lesssim 0.6$ ,  $\overline{T_K} \lesssim 10^3 \text{ K}$ ,  $f_{\text{heat}} \lesssim 0.6$ ,  $R_{\text{peak}}^{\text{heat}} \lesssim 10 h^{-1} \text{ Mpc}$ ,  $\Delta R_{\text{FWHM}}^{\text{heat}} \lesssim 30 h^{-1} \text{ Mpc}$ .

The limits on the IGM parameters are similar at all redshifts considered in this study, indicating that certain IGM states correspond to large amplitudes of the large-scale power spectra and thus are more easily ruled out by the upper limits on the 21-cm signal power spectrum. More stringent upper limits will provide stronger constraints on the IGM parameters. In addition, combining these with other observational constraints such as the observation of the global 21-cm signal and high- $z$  galaxies will strengthen the understanding of the IGM during the EoR.

## ACKNOWLEDGEMENTS

We would like to thank the anonymous referee for insightful comments. We thank Cathryn M. Trott for providing the lists of the MWA upper limits and the corresponding errors, and Bradley Greig for useful discussion related to this work. We acknowledge that the results in this paper have been achieved using the PRACE Research Infrastructure resources Curie based at the Très Grand Centre de Calcul (TGCC) operated by CEA near Paris, France and Marenstrum based in the Barcelona Supercomputing Center, Spain. Time on these resources was awarded by PRACE under PRACE4LOFAR grants 2012061089 and 2014102339 as well as under the Multi-scale Reionization grants 2014102281 and 2015122822. The computations were partly enabled by resources provided by the Swedish National Infrastructure for Computing (SNIC) at PDC partially funded by the Swedish Research Council through grant agreement no. 2018-05973. RG and SZ furthermore acknowledge support by the Israel Science Foundation (grant no. 255/18). GM is supported by Swedish Research Council grants 2016-03581 and 2020-04691.

## DATA AVAILABILITY

The derived data generated in this research will be shared on reasonable request to the corresponding authors.

## REFERENCES

- Bañados E., et al., 2018, *Nature*, **553**, 473  
 Barkana R., 2018, *Nature*, **555**, 71  
 Barkana R., Loeb A., 2005, *ApJ*, **626**, 1  
 Barry N., Hazelton B., Sullivan I., Morales M. F., Pober J. C., 2016, *MNRAS*, **461**, 3135  
 Barry N., et al., 2019, *ApJ*, **884**, 1  
 Behroozi P. S., Silk J., 2015, *ApJ*, **799**, 32

- Bonaldi A., Brown M. L., 2015, *MNRAS*, **447**, 1973
- Bowman J. D., Rogers A. E. E., 2010, *Nature*, **468**, 796
- Bowman J. D., Rogers A. E. E., Monsalve R. A., Mozdzen T. J., Mahesh N., 2018, *Nature*, **555**, 67
- Bradley R. F., Tauscher K., Rapetti D., Burns J. O., 2019, *ApJ*, **874**, 153
- Chapman E., Zaroubi S., Abdalla F. B., Dulwich F., Jelić V., Mort B., 2016, *MNRAS*, **458**, 2928
- Cheng C., et al., 2018, *ApJ*, **868**, 26
- Chornock R., Berger E., Fox D. B., Lunnan R., Drout M. R., Fong W.-f., Laskar T., Roth K. C., 2013, *ApJ*, **774**, 26
- Cohen A., Fialkov A., Barkana R., Monsalve R. A., 2020, *MNRAS*, **495**, 4845
- Datta K. K., Bharadwaj S., Choudhury T. R., 2007, *MNRAS*, **382**, 809
- Datta A., Bowman J. D., Carilli C. L., 2010, *ApJ*, **724**, 526
- Davies F. B., et al., 2018, *ApJ*, **864**, 142
- Dawoodbhoy T., et al., 2018, *MNRAS*, **480**, 1740
- DeBoer D. R., et al., 2017, *Publications of the Astronomical Society of the Pacific*, **129**, 045001
- Dixon K. L., Iliev I. T., Mellema G., Ahn K., Shapiro P. R., 2016, *Monthly Notices of the Royal Astronomical Society*, **456**, 3011
- Dowell J., Taylor G. B., 2018, *ApJ*, **858**, L9
- Draine B. T., Miralda-Escudé J., 2018, *ApJ*, **858**, L10
- Eastwood M. W., et al., 2019, *AJ*, **158**, 84
- Ewall-Wice A., Chang T. C., Lazio J., Doré O., Seiffert M., Monsalve R. A., 2018, *ApJ*, **868**, 63
- Fan X., et al., 2006, *AJ*, **132**, 117
- Feng C., Holder G., 2018, *ApJ*, **858**, L17
- Fialkov A., Barkana R., 2019, *MNRAS*, **486**, 1763
- Fialkov A., Barkana R., Cohen A., 2018, *Physical Review Letters*, **121**, 011101
- Fioc M., Rocca-Volmerange B., 1997, *A&A*, **326**, 950
- Fixsen D. J., et al., 2011, *ApJ*, **734**, 5
- Foreman-Mackey D., Hogg D. W., Lang D., Goodman J., 2013, *PASP*, **125**, 306
- Furlanetto S. R., Oh S. P., Briggs F. H., 2006, *Phys. Rep.*, **433**, 181
- Gehlot B. K., et al., 2019, *MNRAS*, **488**, 4271
- Gehlot B. K., et al., 2020, *MNRAS*, **499**, 4158
- Ghara R., Choudhury T. R., 2020, *MNRAS*, **496**, 739
- Ghara R., Mellema G., 2020, *MNRAS*, **492**, 634
- Ghara R., Choudhury T. R., Datta K. K., 2015a, *MNRAS*, **447**, 1806
- Ghara R., Datta K. K., Choudhury T. R., 2015b, *MNRAS*, **453**, 3143
- Ghara R., Choudhury T. R., Datta K. K., 2016, *MNRAS*, **460**, 827
- Ghara R., Choudhury T. R., Datta K. K., Choudhuri S., 2017, *MNRAS*, **464**, 2234
- Ghara R., Mellema G., Giri S. K., Choudhury T. R., Datta K. K., Majumdar S., 2018, *MNRAS*, **476**, 1741
- Ghara R., et al., 2020, *MNRAS*, **493**, 4728
- Giri S. K., PhD thesis, Stockholm University, Department of Astronomy, 2019, p. 68, ISBN 978-91-7797-611-0
- Giri S. K., Mellema G., 2020, arXiv e-prints, p. arXiv:2012.12908
- Giri S. K., Mellema G., Dixon K. L., Iliev I. T., 2018a, *MNRAS*, **473**, 2949
- Giri S. K., Mellema G., Ghara R., 2018b, *MNRAS*, **479**, 5596
- Giri S. K., Mellema G., Aldheimer T., Dixon K. L., Iliev I. T., 2019a, *MNRAS*, **489**, 1590
- Giri S. K., D'Aloisio A., Mellema G., Komatsu E., Ghara R., Majumdar S., 2019b, *Journal of Cosmology and Astro-Particle Physics*, **2019**, 058
- Greig B., Mesinger A., 2015, *Monthly Notices of the Royal Astronomical Society*, **449**, 4246
- Greig B., Mesinger A., 2017, *MNRAS*, **472**, 2651
- Greig B., Mesinger A., Haiman Z., Simcoe R. A., 2017, *MNRAS*, **466**, 4239
- Greig B., Mesinger A., Bañados E., 2019, *MNRAS*, **484**, 5094
- Greig B., Trott C. M., Barry N., Mutch S. J., Pindor B., Webster R. L., Wyithe J. S. B., 2021a, *MNRAS*, **500**, 5322
- Greig B., et al., 2021b, *MNRAS*, **501**, 1
- Gupta Y., et al., 2017, *Current Science*, **113**, 707
- Harker G., et al., 2009, *MNRAS*, **397**, 1138
- Hasegawa K., Semelin B., 2013, *MNRAS*, **428**, 154
- Hills R., Kulkarni G., Meerburg P. D., Puchwein E., 2018, *Nature*, **564**, E32
- Hinshaw G., et al., 2013, *ApJS*, **208**, 19
- Hothi I., et al., 2021, *MNRAS*, **500**, 2264
- Islam N., Ghara R., Paul B., Choudhury T. R., Nath B. B., 2019, *MNRAS*, **487**, 2785
- Jensen H., et al., 2013, *MNRAS*, **435**, 460
- Kamran M., Ghara R., Majumdar S., Mondal R., Mellema G., Bharadwaj S., Pritchard J. R., Iliev I. T., 2021, *MNRAS*, **502**, 3800
- Kapahtia A., Chingambam P., Ghara R., Appleby S., Choudhury T. R., 2021, arXiv e-prints, p. arXiv:2101.03962
- Kern N. S., Parsons A. R., Dillon J. S., Lanman A. E., Fagnoni N., de Lera Acedo E., 2019, *ApJ*, **884**, 105
- Kolopanis M., et al., 2019, *ApJ*, **883**, 133
- Krause F., Thomas R. M., Zaroubi S., Abdalla F. B., 2018, *New Astron.*, **64**, 9
- Liu A., Parsons A. R., Trott C. M., 2014, *Phys. Rev. D*, **90**, 023019
- Madau P., Meiksin A., Rees M. J., 1997, *ApJ*, **475**, 429
- Majumdar S., Bharadwaj S., Choudhury T. R., 2012, *MNRAS*, **426**, 3178
- Majumdar S., Datta K. K., Ghara R., Mondal R., Choudhury T. R., Bharadwaj S., Ali S. S., Datta A., 2016, *Journal of Astrophysics and Astronomy*, **37**, 32
- McGreer I. D., Mesinger A., D'Odorico V., 2015, *MNRAS*, **447**, 499
- Mebane R. H., Mirocha J., Furlanetto S. R., 2020, *Monthly Notices of the Royal Astronomical Society*, **493**, 1217
- Mellema G., Koopmans L., Shukla H., Datta K. K., Mesinger A., Majumdar S., 2015, *Advancing Astrophysics with the Square Kilometre Array (AASKA14)*, p. 10
- Mertens F. G., Ghosh A., Koopmans L. V. E., 2018, *MNRAS*, **478**, 3640
- Mertens F. G., et al., 2020, *MNRAS*, **493**, 1662
- Mesinger A., Furlanetto S., 2007, *ApJ*, **669**, 663
- Mevius M., et al., 2016, *Radio Science*, **51**, 927
- Mineo S., Gilfanov M., Sunyaev R., 2012, *MNRAS*, **419**, 2095
- Mitra S., Choudhury T. R., Ferrara A., 2015, *MNRAS*, **454**, L76
- Mondal R., et al., 2020, *MNRAS*, **498**, 4178
- Monsalve R. A., Rogers A. E. E., Bowman J. D., Mozdzen T. J., 2017, *ApJ*, **835**, 49
- Monsalve R. A., Greig B., Bowman J. D., Mesinger A., Rogers A. E. E., Mozdzen T. J., Kern N. S., Mahesh N., 2018, *ApJ*, **863**, 11
- Muñoz J. B., Loeb A., 2018, arXiv e-prints, p. arXiv:1802.10094
- Nambissan J., et al., 2021, *Experimental Astronomy*, **1572-9508**
- Ouchi M., et al., 2010, *ApJ*, **723**, 869
- Paciga G., et al., 2013, *MNRAS*, **433**, 639
- Park J., Mesinger A., Greig B., Gillet N., 2019, *Monthly Notices of the Royal Astronomical Society*, **484**, 933
- Parsons A. R., et al., 2014, *ApJ*, **788**, 106
- Patil A. H., et al., 2017, *ApJ*, **838**, 65
- Patra N., Subrahmanyam R., Sethi S., Udaya Shankar N., Raghunathan A., 2015, *ApJ*, **801**, 138
- Philip L., et al., 2019, *Journal of Astronomical Instrumentation*, **8**, 1950004
- Planck Collaboration et al., 2020, *A&A*, **641**, A6
- Price D. C., et al., 2018, *MNRAS*, **478**, 4193
- Pritchard J. R., Loeb A., 2012, *Reports on Progress in Physics*, **75**, 086901
- Rasmussen C. E., Williams C. K. I., 2006, *Gaussian Processes for Machine Learning*. The MIT Press, 2006. ISBN 0-262-18253-X
- Reis I., Fialkov A., Barkana R., 2020a, *MNRAS*, **499**, 5993
- Reis I., Fialkov A., Barkana R., 2020b, *MNRAS*, **499**, 5993
- Ross H. E., Dixon K. L., Ghara R., Iliev I. T., Mellema G., 2019, *MNRAS*, **487**, 1183
- Ross H. E., Giri S. K., Dixon K. L., Ghara R., Iliev I. T., Mellema G., 2020, arXiv e-prints, p. arXiv:2011.03558
- Schneider A., Giri S., Mirocha J., 2020, arXiv e-prints, p. arXiv:2011.12308
- Singh S., Subrahmanyam R., 2019, *ApJ*, **880**, 26
- Singh S., et al., 2017, *ApJ*, **845**, L12
- Sokolowski M., et al., 2015, *Publ. Astron. Soc. Australia*, **32**, e004
- Sun G., Furlanetto S. R., 2016, *MNRAS*, **460**, 417
- Tashiro H., Kadota K., Silk J., 2014, *Phys. Rev. D*, **90**, 083522
- Thomas R. M., Zaroubi S., 2008, *MNRAS*, **384**, 1080
- Thomas R. M., Zaroubi S., 2011, *MNRAS*, **410**, 1377
- Thomas R. M., et al., 2009, *MNRAS*, **393**, 32



- Tingay S. J., et al., 2013, [Publications of the Astronomical Society of Australia \(PASA\)](#), 30, 7
- Trott C. M., et al., 2020, [MNRAS](#), 493, 4711
- Virtanen P., et al., 2020, [Nature Methods](#), 17, 261
- Voytek T. C., Natarajan A., Jáuregui García J. M., Peterson J. B., López-Cruz O., 2014, [ApJ](#), 782, L9
- Wang F., et al., 2020, [ApJ](#), 896, 23
- Watson W. A., Iliev I. T., D’Aloisio A., Knebe A., Shapiro P. R., Yepes G., 2013, [Monthly Notices of the Royal Astronomical Society](#), 433, 1230
- Wayth R. B., et al., 2018, [Publ. Astron. Soc. Australia](#), 35, 33
- Weiser A., Zarantonello S. E., 1988, *Mathematics of Computation*, 50, 189
- Wise J. H., Demchenko V. G., Halicek M. T., Norman M. L., Turk M. J., Abel T., Smith B. D., 2014, [MNRAS](#), 442, 2560
- Yang J., et al., 2020, [ApJ](#), 904, 26
- Zarka P., Girard J. N., Tagger M., Denis L., 2012, in Boissier S., de Laverny P., Nardetto N., Samadi R., Valls-Gabaud D., Wozniak H., eds, SF2A-2012: Proceedings of the Annual meeting of the French Society of Astronomy and Astrophysics. pp 687–694
- Zaroubi S., 2013, in Wiklind T., Mobasher B., Bromm V., eds, *Astrophysics and Space Science Library* Vol. 396, The First Galaxies. p. 45 ([arXiv:1206.0267](#)), [doi:10.1007/978-3-642-32362-1\\_2](#)
- van Haarlem M. P., et al., 2013, [Astronomy & Astrophysics](#), 556, A2

This paper has been typeset from a  $\text{\LaTeX}$  file prepared by the author.